INSTITUTE OF PHYSICS PUBLISHING JOURNAL OF PHYSICS B: ATOMIC, MOLECULAR AND OPTICAL PHYSICS

J. Phys. B: At. Mol. Opt. Phys. **36** (2003) 4889–4910 PII: S0953-4075(03)69156-X

Low energy superelastic scattering from the 4 $^1P_1$ state of calcium in an (e, 2e) spectrometer

Andrew James Murray and Danica Cvejanovic

Schuster Laboratory, The University of Manchester, Manchester M13 9PL, UK

E-mail: Andrew.Murray@man.ac.uk

Received 16 September 2003
Published 21 November 2003
Online at stacks.iop.org/JPhysB/36/4889

Abstract

Atomic collision parameters have been derived for electron impact excitation of calcium using the superelastic scattering method, at incident energies equivalent to 20, 25 and 35 eV. The pseudo-Stokes parameters for the superelastic process were determined, and the parameters $P^+_{\rm lin}$, $L^+_\perp$, γ^+ and $P^+_{\rm tot}$ derived for the 4 ^{1}P$_1$ state. The results are compared to a relativistic distorted-wave approximation (RDWA) theory, and to previous experimental results. At the highest incident energy the results presented here compare well with theory, but at the lowest energy, significant disagreement between theory and experiment is observed.

S This article has associated online supplementary data files

1. Introduction

The derivation of atomic collision parameters (ACPs) from electron excitation of atoms has a long and distinguished history [1, 2], and provides one of the most sensitive tests of scattering theories for the excitation of atoms. In contrast to the direct evaluation of the differential inelastic scattering cross section which provides information on the excitation probability as a function of scattering angle, these relative measurements determine the internal structure of the excited atom following electron excitation. As such, they allow the relative amplitudes and phases of the contributing scattering amplitudes to be determined.

There are two principal experimental methods used to determine these ACPs. The first method, developed by Kleinpoppen and colleagues [3] and later modified by Standage and Kleinpoppen [4], uses a coincidence technique to measure the correlated signal between the inelastically scattered electron that excited the atom, and the photon that is spontaneously emitted from the excited target. These experiments either directly determine the angular distribution of the correlated photons (a method usually employed for high energy photons as emitted by the n ^{1}P$_1$ states of helium or neon), or measure the polarization of the photons emitted in coincidence.

Measurement of the angular distribution of the emitted photons cannot experimentally determine the complete information about the state (and hence the scattering amplitudes), since these experiments do not measure the circular component of the radiation. By contrast, measurement of the Stokes parameters of the emitted radiation from an excited P-state allows a complete set of collision parameters to be independently determined. Since the Stokes parameters yield a description of the ellipticity of the emitted radiation, the 'shape' of the excited atom that produced the radiation can be determined. This method has also been applied to electron excitation of D-states [5, 6], however it is not possible to unambiguously determine a complete description of the excited state without additional measurements or assumptions being made [7].

The second method that is used to determine the ACPs is the superelastic scattering method first demonstrated by Hertel and colleagues [8, 9], and which has been employed by a number of experimental groups since this time [10–33]. In these experiments, time reversal arguments are employed to extract the ACPs. For the simplest case of S- to P-state excitation, photons are initially directed onto the target from a tuneable, polarized, single mode laser beam whose energy is made resonant between the ground S-state and the excited P-state. The target atom absorbs the photon, and is excited coherently to a specific state in the P-state manifold. The state that is excited depends on the laser beam parameters, including the intensity, polarization and frequency of the laser beam with respect to the atomic beam [15, 29].

Following laser excitation the target is then subjected to the incident electron beam. Three processes may then occur. The electron beam may be elastically scattered, the electrons may be inelastically scattered thereby promoting the atom to a higher lying state, or the target may de-excite to a lower state (usually the ground state), the electrons emerging from the reaction with greater energy than in the incident beam. In the latter case, the electrons are said to be superelastically scattered. The probability of superelastic scattering in any given direction depends on the 'shape' of the target prior to the collision, which is determined by the optical pumping process.

Super-elastic electron scattering can therefore be considered as the 'time reversal' of the electron–photon coincidence method, provided that the correct momenta of the scattered and incident electron are observed. To ensure this, the electron source and electron detector used for coincidence measurement are exchanged, the laser beam is injected in the opposite direction to the photon detected in coincidence, and the energy of the incident electron is set to that of the detected electron in the coincidence experiment. Since the process is one of superelastic scattering, the detected electron emerges from the reaction with the same energy as the incident electron in a coincidence measurement.

The advantage of the superelastic scattering method over the coincidence technique arises since the laser beam is highly directed, and the resonant photon flux is very high. The probability of laser excitation followed by electron de-excitation is therefore also high, with typical yields ranging from Hz to kHz. This high yield allows the superelastically scattered electron flux to be determined over a wide range of scattering angles as a function of the laser polarization, from which a set of 'pseudo-Stokes' parameters are derived [34]. The pseudo-Stokes parameters can then be directly related to conventional Stokes parameters obtained from coincidence measurements by considering the optical pumping of the atom under the influence of the laser radiation [35]. The experiment therefore reduces to that of determining the count rate of the superelastically scattered electrons at a given angle as a function of the laser polarization.

By contrast, the coincidence technique measures the inelastically scattered electron, then waits for a time-correlated photon to arrive at the photon detector after polarization analysis. Since most of the spontaneously emitted photons do not travel towards the detector, this process

is very slow. Further, since the probability of excitation of the state (as given by the differential cross section) reduces markedly as the scattering angle increases, the yield of correlated events also reduces. For this reason, most electron–photon coincidence studies are confined to lower scattering angles where the cross section is high. At larger scattering angles, the stability of the apparatus over the very long accumulation times which are required becomes the determining factor in the success of the experiment.

Whilst the superelastic method has many attractions, there are also significant limitations to this method. The principal constraint is due to the limited availability of single mode high quality laser radiation sources. The radiation needs to have excellent frequency stability, must be coherent and have high power. Sources which have been used include continuous wave (CW) dye lasers [8–28, 30–32], CW Ti:sapphire lasers [29] and external cavity diode lasers [33]. All of these sources produce a limited range of wavelengths, with photon energies ranging from ∼1 eV through to ∼3 eV. Since the majority of atomic targets have their first excited state above this range, the superelastic technique cannot be used and conventional electron–photon coincidence methods must be adopted. For this reason, the superelastic method has been constrained mostly to the alkali targets (see [8–15, 17, 18, 23–29, 33]), and more recently to the alkali-earth targets (see [16, 19–22, 30–32]).

In the experiments described in this paper, the superelastic scattering method has been used to determine the ACPs for excitation of the 4 $^1P_1$ state of calcium at energies ranging from 20 to 35 eV. Calcium has been studied previously using a CW dye laser by Teubner and colleagues [21, 22], however the results were over a limited range of energies (25.7 and 45 eV) and scattering angles (3°–100°). These limitations arose due to the difficulty of producing stable high power radiation from a dye laser at the required wavelength of ∼423 nm. At this wavelength laser dyes are expensive and quickly degrade, a UV argon ion laser is needed to pump the dye laser and the low output power of the dye laser (typically ∼50 mW) makes it difficult to operate the laser reliably in single mode.

By contrast, the experiments described here used a high power CW Ti:sapphire laser followed by an external intra-cavity doubler to produce the desired radiation, with a laser power in excess of 120 mW at 423 nm. The stability of the radiation is controlled by the Ti:sapphire laser, which is frequency-locked to an external Fabry–Perot etalon. The linewidth of the doubled radiation was around 200 kHz and was single mode. The high power of the 423 nm radiation allowed measurements to be conducted over the complete range of scattering geometries accessible to the electron spectrometer, ranging from 35° through to 125°.

It should be noted that the experiments described here were not conducted in a vacuum chamber designed for superelastic measurements, but were carried out in the Manchester (e, 2e) spectrometer which was commissioned to study ionization processes using coincidence techniques [36–39]. The (e, 2e) spectrometer at Manchester has recently been modified to carry out ionization studies of laser excited calcium atoms [40], and the superelastic scattering studies described here were conducted as part of the optimization procedure for the spectrometer prior to commencing these difficult (e, 2e) experiments. By measuring the superelastic yield from laser excited targets, it is possible to ensure that the laser beam, atomic beam and electron optics are optimally aligned to a common interaction region inside the vacuum chamber, which is essential for these future (e, 2e) coincidence studies.

The results presented here at 25 eV equivalent incident energy are compared to the superelastic scattering results of Law and Teubner [21], and to the electron–photon coincidence work of El-Fayoumi *et al* [41] at 25.7 eV. Law and Teubner [21] and Zohny *et al* [42] also conducted studies at 45 eV equivalent incident energy, however the spectrometer at Manchester cannot access this energy without modification, and so no comparison can be made. The electron–photon coincidence studies at 25.7 eV [41] were confined to scattering angles between

15° and 40°, whereas the superelastic scattering results were taken over a range of scattering angles between 5° and 100°. The (e, 2e) apparatus at Manchester cannot access scattering angles below 35° due to the position of the Faraday cup, and cannot access angles above 125° due to the position of the electron gun. Hence all measurements presented here were conducted between these angles.

Theoretical calculations of the ACPs for calcium are limited to the published work of Stauffer and colleagues [43, 44], who derived the complete set of parameters using a RDWA model, and those of Clark and Csanak who used a distorted-wave approximation (DWA) and first-order many-body theory (FOMBT) model to calculate $L_{\perp}^{+}$ at 25.7 eV [21]. The calculations of [43, 44] were carried out at incident energies of 20.7, 25.7 and 35.7 eV allowing a close comparison to be made with the new results presented here. At the higher energies, excellent agreement is found between experiment and theory, but as the energy decreases, significant deviations are seen.

This paper is divided into five sections. The superelastic scattering process is described in section 2 together with the laser pumping process for calcium under the conditions used in this experiment. The experimental apparatus is described in section 3, together with the techniques adopted to measure the pseudo-Stokes parameters in the (e, 2e) experiment. The Stokes parameters and derived ACPs are presented in section 4 and compared to theoretical calculations and previous experimental results. Conclusions are drawn from these comparisons in section 5, and future work to be carried out in this area is discussed.

2. The superelastic scattering process

Figure 1 shows the scattering geometry of the (e, 2e) experiment which was adapted for these superelastic scattering studies. In contrast to conventional methods, the electron gun in the (e, 2e) spectrometer cannot move in the coplanar detection plane, and so the analyser is rotated around the scattering plane. The quantization axis for the superelastic process in the natural frame of reference is orthogonal to the scattering plane and is in the opposite direction to the incident laser beam, whereas the x-axis in this frame is given by the direction of the scattered electron. The x-axis in the natural frame therefore moves in the scattering plane with respect to the laboratory frame of reference as the analyser is rotated. The laser beam entered the spectrometer orthogonal to the scattering plane, the polarization of the laser beam being determined by a Glan Taylor linear polarizer followed by a zero-order $\lambda/2$ retardation plate for linear polarization studies, and a zero-order $\lambda/4$ retardation plate for circular polarization studies.

In the natural frame of reference, the electron excited $4\,{}^1\mathrm{P}_1$ state of calcium can be described by four independent ACPs $L_{\perp}^{+}$, P_{lin}^{+}, γ^{+} and ρ_{00}. $L_{\perp}^{+}$ indicates the expectation value of the angular momentum of the state orthogonal to the scattering plane. P_{lin}^{+} and γ^{+} determine the alignment of the P-state in the scattering plane, where P_{lin}^{+} indicates the length to width ratio of the aligned state and γ^{+} indicates the alignment angle with respect to the natural frame x-axis. The parameter ρ_{00} describes the 'height' of the charge cloud out of the scattering plane at the origin, a positive value indicating either electron exchange or the breakdown of LS coupling has occurred during the interaction. The superscript '+' on the parameters indicates positive reflection symmetry in the scattering plane. Finally, the derived parameter $P_{\mathrm{tot}}^{+} = \sqrt{P_{\mathrm{lin}}^{+2} + L_{\perp}^{+2}}$ indicates the degree of polarization, which is a measure of the coherence of the scattering process. When $P_{\mathrm{tot}}^{+} = 1$, the interaction is completely coherent. A schematic of the charge cloud in the scattering plane indicating these parameters is shown in figure 1.

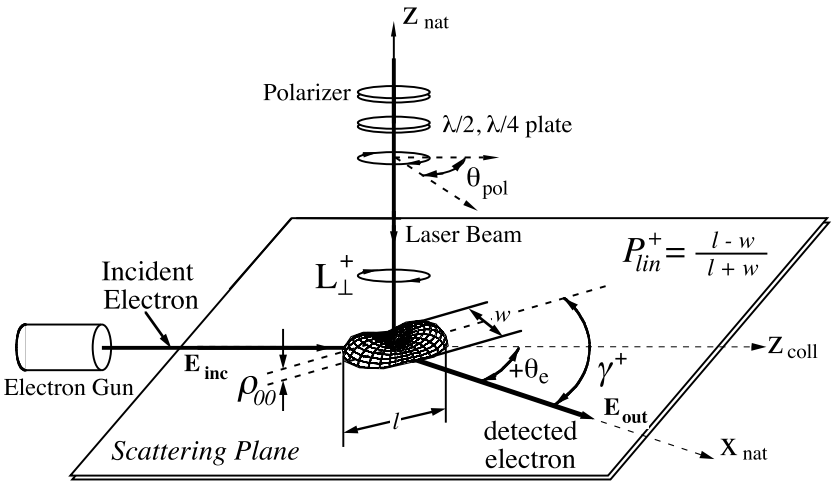

Figure 1. The superelastic scattering geometry adopted in the (e, 2e) spectrometer. The electron gun is fixed in space, and the analyser moves around the scattering plane. The ACPs are shown for a P-state in the natural frame. The laser beam for superelastic scattering experiments enters along the $z_{\rm nat}$ axis, whereas the $x_{\rm nat}$ axis is along the direction of the scattered electron. The natural frame therefore rotates around the scattering plane as the analyser position is changed.

To obtain values of the four ACPs from the superelastic scattering experiment, it is necessary to make four independent measurements. Three measurements are required with the laser radiation orthogonal to the scattering plane to determine the parameters $L^+_\perp$, $P^+_{\rm lin}$ and γ^+, whereas a fourth measurement is required with the laser propagating in the scattering plane to determine ρ_{00}. In the experiments described here, it was not possible to direct the laser radiation into the scattering plane and so only the parameters $L^+_\perp$, $P^+_{\rm lin}$ and γ^+ have been derived.

To determine these parameters, the experiment measures the differential cross section for superelastically scattered electrons as a function of the laser polarization, from which a set of pseudo-Stokes parameters can be derived [35]. These parameters are given by:

$$\begin{aligned} P_1^S(\theta_{\rm e}) &= \frac{S_0(\theta_{\rm e}) - S_{90}(\theta_{\rm e})}{S_0(\theta_{\rm e}) + S_{90}(\theta_{\rm e})} \\ P_2^S(\theta_{\rm e}) &= \frac{S_{45}(\theta_{\rm e}) - S_{135}(\theta_{\rm e})}{S_{45}(\theta_{\rm e}) + S_{135}(\theta_{\rm e})} \\ P_3^S(\theta_{\rm e}) &= \frac{S_{\rm RHC}(\theta_{\rm e}) - S_{\rm LHC}(\theta_{\rm e})}{S_{\rm RHC}(\theta_{\rm e}) + S_{\rm LHC}(\theta_{\rm e})} \end{aligned} \tag{1}$$

where $S_\kappa(\theta_{\rm e})$ represents the superelastic yield at the scattering angle $\theta_{\rm e}$ for the laser linearly polarized at angle κ with respect to the natural frame x-axis, or in the case of the P_3^S parameter, κ represents right or left hand circularly polarized light.

2.1. The laser pumping process

To ascertain the relationship between the pseudo-Stokes parameters and the conventional Stokes parameters derived from coincidence studies, it is necessary to determine the effects of optical pumping on the excited target prior to electron de-excitation. For alkali targets, the interaction of the laser with the atom couples through hyperfine state transitions, which makes the interaction process complex since many states contribute to the optical pumping. Models

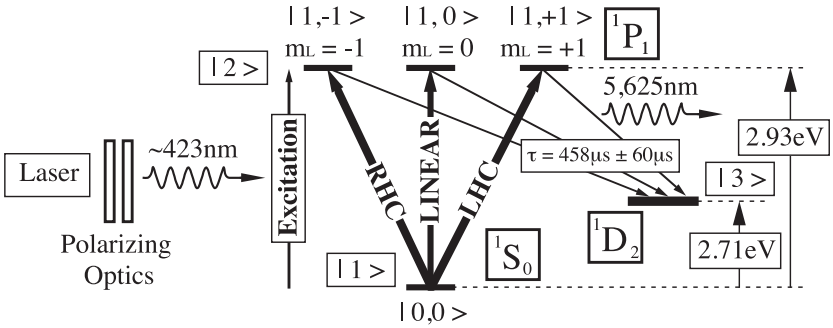

Figure 2. Excitation of calcium from the 4 $^1S_0$ state to the 4 $^1P_1$ state by radiation at ∼423 nm (2.93 eV). In the laser frame, linearly polarized radiation excites the $|1, 0\rangle$ state whereas circularly polarized radiation excites the $|1, \pm 1\rangle$ states. The 4 $^1D_2$ metastable state lies below the 4 $^1P_1$ state at an energy of 2.71 eV, and so acts as a sink for laser excited atoms which spontaneously emit radiation at 5.625 μm. The branching ratio between the 4 $^1D_2$ and 4 $^1S_0$ states is 1:10^5.

of optical pumping have been developed since Hertel and Stoll used a simple rate equation approach to derive these effects [8, 9]. Since this time, a more sophisticated semi-classical theory has been derived [45], as well as a full quantum electro-dynamic model [15]. These models have been exhaustively tested against experiment, and the QED model has been found to produce more exact results compared to the semi-classical or rate equation models [46]. This agreement occurs since the equations of motion in the QED model can be rigorously derived from a general set of equations, within the usual constraint that the rotating wave and dipole approximations are valid [47].

The QED model has therefore been used here to ascertain the dynamics of the excited state of calcium. Calcium is an alkali earth element, has no significant isotopes other than the naturally occurring isotope ^{40}Ca, and so has no hyperfine structure. The atom can therefore be well represented using LS coupling.

Figure 2 shows the laser excitation scheme for calcium where the quantization axis is chosen to be along the direction of the laser polarization vector. For linearly polarized radiation, only the $|L, m_L\rangle = |1, 0\rangle$ state is excited in this reference frame. For circularly polarized light, the quantization axis is chosen to be along the direction of laser propagation and the states $|L, m_L\rangle = |1, \pm 1\rangle$ are selectively excited by left and right hand polarized light respectively. The intermediate 4 $^1D_2$ state lies between the 4 $^1P_1$ state and the 4 $^1S_0$ ground state, and since transitions to this state from the 4 $^1P_1$ state are optically allowed, this state will act as a 'sink' to reduce the effective population of the excited targets. In the laser reference frame, Rabi cycling therefore occurs between the $|0, 0\rangle$ ground state and only one of the $|1, m_L\rangle$ excited states, depending on the polarization of the laser.

Spontaneous emission can occur from the $|1, m_L\rangle$ excited state either back to the ground state, or to the intermediate 4 $^1D_2$ state at which time the atom no longer participates in the laser interaction. The optical pumping therefore reduces to a simple three-state system in this reference frame:

$$\begin{aligned}
\dot{\rho}_{11}(t) &= \mathrm{i}(\rho_{12}(t) - \rho_{21}(t)) + \Gamma_{21}\rho_{22}(t) \\
\dot{\rho}_{22}(t) &= \mathrm{i}(\rho_{21}(t) - \rho_{12}(t)) - \Gamma_{21}\rho_{22}(t) - \Gamma_{23}\rho_{22}(t) \\
\dot{\rho}_{12}(t) &= \mathrm{i}(\rho_{11}(t) - \rho_{22}(t)) - \left(\tfrac{1}{2}(\Gamma_{21} + \Gamma_{23}) + \mathrm{i}\delta\right)\rho_{12}(t) \\
\dot{\rho}_{21}(t) &= \mathrm{i}(\rho_{22}(t) - \rho_{11}(t)) - \left(\tfrac{1}{2}(\Gamma_{21} + \Gamma_{23}) - \mathrm{i}\delta\right)\rho_{21}(t) \\
\rho_{11}(t) + \rho_{22}(t) + \rho_{33}(t) &= 1; \qquad \rho_{11}(0) = 1.
\end{aligned} \tag{2}$$

The equations of motion for this system given in equation (2) above have been determined from the QED model in a straightforward way. In these equations ρ_{11} represents the population of the ground state, ρ_{22} the population of the $|1, m_L\rangle$ excited state, ρ_{33} the total population of the 4 ^{1}D$_2$ state due to spontaneous emission, and $\rho_{12} = \rho_{21}^*$ are optical coherences generated by the laser interaction. The total population is normalized to unity.

The dynamics of the interaction depends on the lifetime of the upper state, the branching ratio of the decay rates Γ_{21}/Γ_{23} for spontaneous emission to the 4 ^{1}S$_0$ and 4 ^{1}D$_2$ states, the intensity $I_{\rm las}$ of the laser radiation and the relative detuning δ of the laser radiation from line resonance. The intensity is given by the half-Rabi frequency:

$$\Omega_{21} = \eta\sqrt{I_{\rm las}} = 9.95 \times 10^7\sqrt{I_{\rm las}}\ \text{rad s}^{-1} \tag{3}$$

where $I_{\rm las}$ is in mW mm^{-2}. The frequency doubled laser beam at 423 nm has an approximately Gaussian intensity profile, whereas the detuning δ is governed by the Doppler profile of the atomic beam.

The lifetime of the 4 ^{1}P$_1$ excited state of calcium has been determined to be $\Gamma_2^{-1} = (\Gamma_{21} + \Gamma_{23})^{-1} = 4.6$ ns, whereas the branching ratio has been measured to be $\Gamma_{21}/\Gamma_{23} = (1.0 \pm 0.015) \times 10^5$ [48]. Solving equation (2) over a range of different intensities and detunings appropriate to the experimental apparatus indicates that for the time the atoms are within the $\sim$1 mm^3 interaction region, less than 0.2% of the total population transfers by spontaneous emission to the 4 ^{1}D$_2$ state. Hence the effects of this transfer can effectively be ignored, and the system to a good approximation can be considered as a two-level system.

Figure 3 shows the dynamics of the upper state population $\rho_{22}(t)$ obtained by solving equations (2) for various laser intensities and detunings. A complete description of the optical pumping process must integrate the signal over the intensity profile of the laser and the Doppler profile of the atomic beam. From figure 3 it is clear that for laser intensities up to 100 mW mm^{-2} and for a Doppler detuning ranging from resonance ($\delta = 0$ MHz) through to $\delta = 500$ MHz, the dynamic variation in $\rho_{22}(t)$ due to Rabi cycling decays rapidly, and equilibrium is reached in less than 50 ns. Since the atoms spend around 2000 ns within the interaction region, to a good approximation the initial variation due to Rabi cycling can be ignored. Further, since the system can be approximated to a two-level system, the equilibrium population can be derived from the steady state solution of equations (2) by taking $\Gamma_{23} = 0$. In this case the solution is analytic and is given by:

$$\rho_{22}(I_{\rm las}, \delta) = \frac{4\Omega_{21}^2}{8\Omega_{21}^2 + \Gamma_2^2 + 4\delta^2} = \frac{4\eta^2 I_{\rm las}}{8\eta^2 I_{\rm las} + \Gamma_2^2 + 4\delta^2}; \qquad \rho_{11} = 1 - \rho_{22}. \tag{4}$$

The effects of the intensity profile of the laser beam and Doppler profile of the atomic beam can then be calculated to establish the excited state population relative to the ground state in the interaction region. Doppler integration is performed using a Gaussian weighting function to reflect the distribution of atoms at any given velocity, the mean velocity being given by [49]:

$$\langle v\rangle = 1.45 \times 10^2\sqrt{\frac{T}{M_{\rm Ca}}}\ \text{m s}^{-1} \tag{5}$$

where T is the temperature of the oven (typically 850 K) and $M_{\rm Ca}$ is the atomic number of calcium, from which the mean velocity is calculated to be 680 m s^{-1}.

Using equation (4) the population of the upper state in the interaction region is estimated by integrating over a cylindrical laser beam which has a Gaussian intensity profile, together with integration over the $\sim$600 MHz Doppler profile measured for the atomic beam [50]. From these calculations, the relative upper state population has been estimated to be 13% of the total population of atoms within the interaction region.

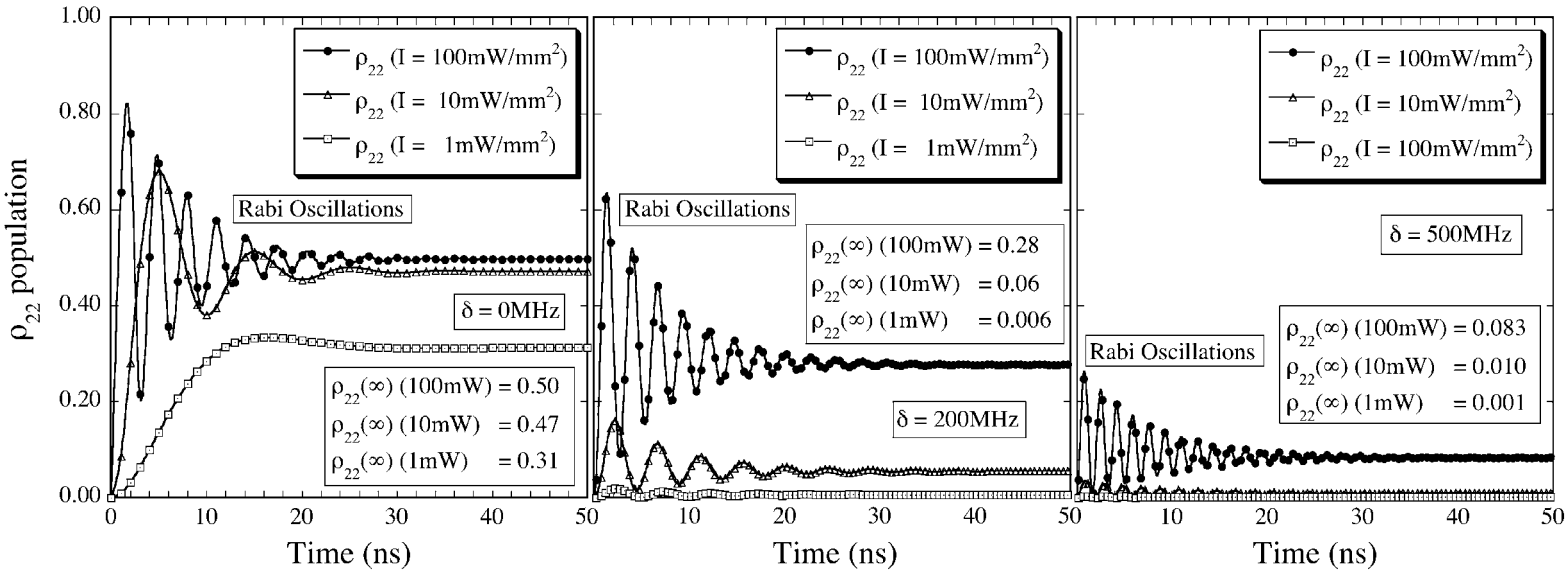

Figure 3. Time dependence of ρ_{22} for various Rabi frequencies and detunings δ relevant to the experiment. The population of the upper state is seen to reach a steady state under all conditions within 50 ns.

The relationship between the pseudo-Stokes parameters and the normal Stokes parameters (and hence ACPs) is particularly simple to derive for S-state to P-state laser excitation, since there are no contributions from fine or hyperfine structures that need to be considered in the optical pumping process. The relationship between these parameters is given by:

$$\begin{aligned} &P_1 = P_1^S; \qquad P_2 = P_2^S; \qquad P_3 = P_3^S \\ &\therefore P_{\text{lin}}^+ = \sqrt{(P_1^S)^2 + (P_2^S)^2}; \qquad \gamma^+ = \frac{1}{2}\tan^{-1}\left(\frac{P_2^S}{P_1^S}\right) \\ &L_\perp^+ = -P_3^S; \qquad P_{\text{tot}}^+ = \sqrt{(P_1^S)^2 + (P_2^S)^2 + (P_3^S)^2}. \end{aligned} \tag{6}$$

3. Experimental technique

As noted in section 1, the experimental apparatus was not designed for superelastic experiments, and these measurements were carried out as part of a new research programme to study ionization from laser excited targets. The spectrometer that was used is the computer controlled and computer optimized (e, 2e) spectrometer at Manchester, which has the flexibility to access a complete set of scattering geometries from a coplanar geometry through to the perpendicular plane. This spectrometer has been detailed in a number of different publications [36–39, 51], and so will only briefly be described here, highlighting the changes that have been made for these new experiments.

Figure 4 shows the apparatus that is used, configured in the perpendicular plane so as to highlight different facets of the spectrometer. The electron gun is a two-stage lens design using a hairpin tungsten cathode to produce an energy resolution around 500 meV. The gun is attached via a 'yoke' to allow the gun to rotate from the perpendicular plane ($\psi = 90°$) through to coplanar geometry ($\psi = 0°$). The analysers rotate in the horizontal detection plane. When the gun is at $\psi = 0°$, the analysers are constrained to be between $\theta_e = 35°$ and 125° by the Faraday cup and electron gun. The analysers comprise a cylindrical molybdenum zoom lens with an opening angle of $\pm 3°$, which focuses the interaction region onto the opening aperture of a hemispherical electrostatic energy analyser. The hemispherical analyser refocuses energy selected electrons onto the entrance cone of a Photonis 919BL channeltron, which detects and amplifies the electrons so as to pass the signal to a rate-meter and counter. In these superelastic scattering experiments, the superelastic scattering signal was detected by analyser 2, with symmetry checks being carried out at selected angles using the signal from analyser 1.

The calcium atoms were produced from an oven located at an angle of 45° to the scattering plane, so as to allow the analysers maximum angular range. The oven was a two-stage resistively heated design which operated at a temperature around 850 K and which used a 35 mm long 0.9 mm ID output nozzle to help direct the atomic beam to the interaction region. The Doppler width at the interaction region was determined to be 600 MHz for this configuration, obtained by observing fluorescence as the laser beam was scanned through resonance. A full description of the oven design is given in [50].

The calcium atoms directed through the interaction region were collected on a conical stainless steel beam dump located opposite the oven (not shown on the diagram). The beam dump was cooled to a temperature of -185 ± 5 °C by passing liquid nitrogen through the mounting assembly that held the beam dump. The liquid nitrogen passed from a dewar located on the top flange of the spectrometer to the dump via flexible stainless steel hoses, the vapour from boil-off being passed back through the dewar to exit the spectrometer. This configuration maintained the beam dump at liquid nitrogen temperatures irrespective of the operating condition of the oven. The lifetime of the 5 litre dewar was

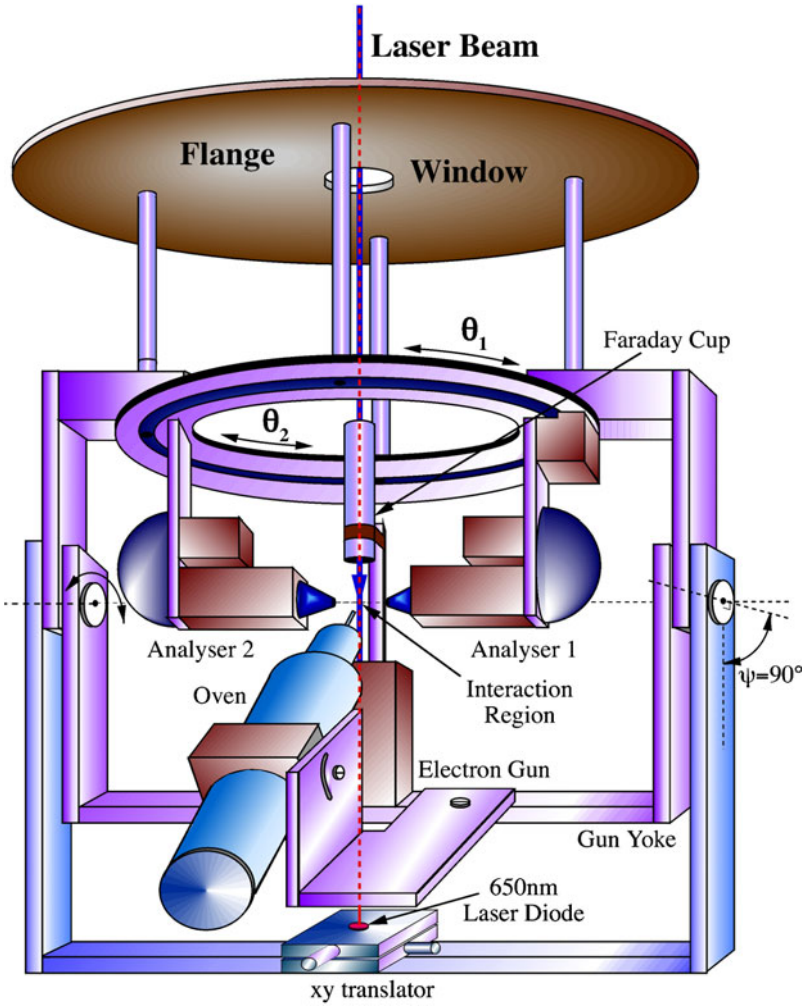

Figure 4. The (e, 2e) spectrometer configured in the perpendicular plane ($\psi = 90°$). All experiments were carried out in a coplanar geometry ($\psi = 0°$). The oven was located at 45° to the electron gun and rotated with the gun and beam dump (not shown on this diagram). The analysers rotate around the horizontal plane, being constrained to be between the Faraday cup and electron gun when $\psi = 0°$. The laser beam entered the chamber through a window on the top flange. A 650 nm diode laser mounted below the electron gun on an xy-translator produced a tracer beam directed through the interaction region and out of the chamber. This tracer beam was used to accurately direct the resonant laser beam to the interaction region.

(This figure is in colour only in the electronic version)

around 6 h when the oven was operating. Full details of the dewar design may be found in [52].

Although most of the atomic beam was collected by the beam dump, thin layers of calcium were deposited onto other surfaces inside the spectrometer. This thin deposition was found to change the contact potentials of the molybdenum and stainless steel surfaces near the interaction region, and so it was necessary to regularly monitor the energy of the electron gun and analysers to correct for this variation. After around five days of continuous emission of calcium from

the oven, the contact potential was found to stabilize, allowing reliable results to be obtained. A stainless steel beam dump was used, as it was found that copper and aluminium strongly reacted with the hot calcium beam to form insulating compounds that would charge up when the electron beam was operating.

The vacuum chamber in which the spectrometer was housed is constructed of 304 grade stainless steel that is lined with a 3 mm thick μ-metal shield both inside the chamber and external to the chamber. This lining was sufficient to reduce external magnetic fields to less than 3 mG at the interaction region. The chamber was pumped by a 500 l s^{-1} turbo-molecular pump located on the bottom flange. Typical operating pressures during operation were 3×10^{-8} Torr, with a background pressure of 1.5×10^{-8} Torr.

The laser system was comprised of a Coherent MBR-110 Ti:sapphire laser which was pumped by a Coherent Verdi–V10 Nd:YVO_4 pump laser operating at 532 nm. The Ti:sapphire laser produced 1500 mW of single mode radiation which was locked to an external reference cavity. The laser operated at a wavelength of 845.3712 nm (in air) as determined by a Burleigh WA-1500 wavemeter.

Radiation from the MBR-110 laser passed through a mode matching telescope and optical isolator to a Coherent MBD-200 enhancement cavity, where radiation at a wavelength of 422.6856 nm was produced. The enhancement cavity produced an output beam with a power around 120 mW, which was directed to the spectrometer via mirrors and a collimating lens. The radiation was passed through a Glan Taylor polarizer to eliminate any ellipticity in the beam generated by slight birefringence of the mirrors, and was then passed through a zero-order $\lambda/2$ plate to control the direction of the polarization vector for linearly polarized radiation, or was passed through a zero-order $\lambda/4$ plate to produce circularly polarized radiation. The resulting light passed through a window located centrally on the top flange of the spectrometer so as to pass through the interaction region.

The laser radiation at $\sim$423 nm was accurately directed orthogonal to the scattering plane and through the interaction region by following light from a tracer beam emitted by a 5 mW laser diode located inside the vacuum chamber. The trace laser operating at $\lambda = 650$ nm was mounted on a plate below the interaction region as shown in figure 4. While the spectrometer was outside the vacuum chamber, the diode laser was accurately positioned using two custom designed vacuum compatible translators so that its beam passed through the interaction region defined by the analysers, electron gun and oven [53]. A 650 nm interference filter was placed in the path of the laser beam directly above the laser diode to protect the laser from damage when the 423 nm laser beam was operating.

The experimental procedure was as follows. The liquid nitrogen dewar was filled and the oven was turned on to a temperature of 200 °C. The electron gun was turned on to emit a current of $\sim$100 nA at this time, and the oven temperature was increased slowly. At an oven temperature of $\sim$400 °C the pressure in the chamber was seen to rise to around 1×10^{-7} Torr, and the current from the gun measured by the Faraday cup correspondingly reduced. A rise in pressure was always observed at this temperature, irrespective of whether the oven had been operated previously and whether the vacuum chamber had been opened. The elevated pressure lasted typically 30 min. After this time the gun current slowly recovered, the pressure decreased back to normal and the temperature of the oven could then be increased. No explanation for this process has been found, but it was found necessary to ensure that the gun only operated at low current prior to the pressure rise, or the electron optics would not then tune correctly.

The temperature of the oven was left to stabilize at around 560 °C and the conditions of the experiment were monitored for several days to establish when the electron spectrometer reached stability. This was done by monitoring the energy loss spectra, and by measuring the energy dependence of the coincidence yield for ionization from calcium in the ground state.

The analysers and electron gun were independently calibrated in energy by measuring resonances in the elastic scattering of helium, and by monitoring resonances in the ionization continuum [54]. The uncertainty in the absolute energy calibration from these measurements was around 0.5 eV.

Once the energy of the system was calibrated, the laser beam was introduced to the system by tracing along the 650 nm laser beam emitted by the internal diode laser. The two beams were made collinear over the 5 m distance from the laser table to the spectrometer, ensuring that the 423 nm laser beam was accurately positioned through the interaction region. The laser was then tuned to resonance by focusing fluorescence through a side window onto an external photodiode.

The laser induced fluorescence was analysed to determine the effects of radiation trapping inside the vacuum chamber. At a temperature of 560 °C, the polarization of the emitted fluorescence was measured to be $98 \pm 3\%$, and so the effects of radiation trapping at this temperature were considered to be negligible. All superelastic measurements were taken at this oven temperature.

Once the laser beam was positioned and tuned, the superelastic signal was optimized at a given scattering angle by focusing the input lenses of the analysers, and by adjusting the electron beam from the gun. Optimization was performed by observing both the scattering rate and the quality of the superelastic spectrum. The laser beam parameters were then fine tuned so as to yield the best superelastic signal.

An example of the energy loss/gain spectrum is shown in figure 5, for a scattering angle $\theta_e = 35°$ at an analyser energy of 35 eV. The spectrum was obtained by scanning the incident electron beam energy. The superelastic signal can easily be seen, showing the good resolution compared to the much larger elastic peak. This resolution was possible due to the relatively large energy of the excited state (2.93 eV) compared to the resolution of the spectrometer. The inelastic signal from the P-state can also be seen.

The superelastic scattering signal was obtained as a function of the polarization of the laser beam in a different way to that usually employed in these types of experiments. Since the analysers moved rather than the electron gun, it was decided to use a $\lambda/2$ plate to rotate the laser polarization vector 360° around the scattering plane in 10° steps. The reference angle for this was set by the direction of the electron beam since this was fixed in the laboratory frame, rather than by the direction of the analysers. The direction of the polarization vector reference angle with respect to the electron beam direction had an uncertainty of $\pm 3°$. Once the superelastic scattering signal was obtained as a function of the angle of the polarization vector, the data was then fitted to a sinusoidal function as detailed in the next section, and the Stokes parameters P_1, P_2 were derived. This method has the additional advantage that P_{lin}^{+} and γ^{+} can be obtained *directly* from the fitting parameters, rather than deriving these from the pseudo-Stokes parameters. The uncertainty in these parameters was therefore correspondingly smaller.

The P_3 pseudo-Stokes parameter was obtained by placing a $\lambda/4$ plate after the Glan Taylor polarizer, and rotating this to obtain circularly polarized radiation. The correct relative angles $\vartheta_{45°}^{\mathrm{ret}}$, $\vartheta_{135°}^{\mathrm{ret}}$, $\vartheta_{-45°}^{\mathrm{ret}}$, $\vartheta_{-135°}^{\mathrm{ret}}$ of the retardation plate with respect to the polarization direction were determined by retro-reflecting the radiation back through the $\lambda/4$ plate and polarizer, rotating the retarder to ensure that the resulting radiation was extinguished. This was checked at all four angles, the degree of circular polarization being determined to be $>99\%$ for all angles. The handedness of the radiation was determined using a Babinet Soleil compensator [55].

For linearly polarized radiation, measurements were obtained at each polarization angle by counting the superelastic signal for 30 s, then repeating the measurement five times to obtain an average count rate together with a statistical variance of the signal. The laser tuning

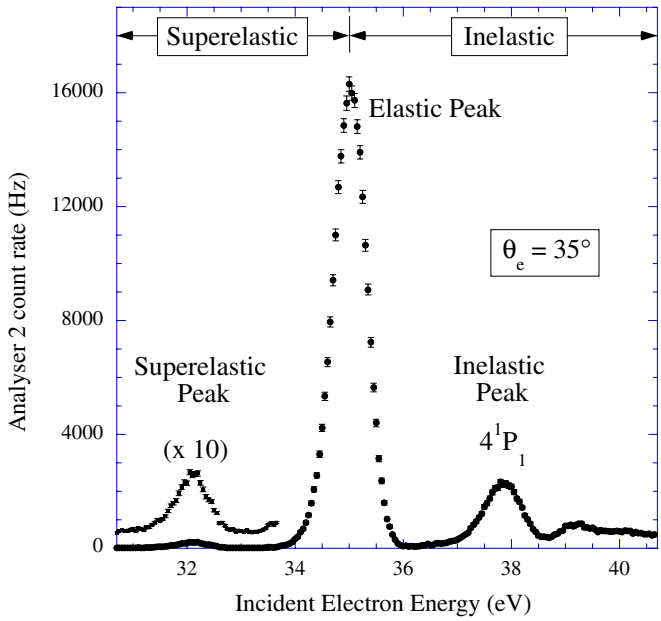

Figure 5. Energy loss/gain spectrum of calcium under the influence of resonant laser radiation. The analyser was fixed at a scattering angle $\theta_e = 35°$ and a pass energy of 35 eV. The energy of the incident electron beam was scanned from 30 eV through to 40 eV so as to pass through the inelastic, elastic and superelastic peaks. The superelastic peak is easily resolved from the elastic peak due to the high excitation energy of the state (2.93 eV) compared to the resolution of the spectrometer (∼1 eV).

was checked regularly during these measurements by monitoring the fluorescence signal and re-adjusting the laser tuning to ensure optimization. This was found to be necessary as the frequency locking system of the Coherent laser system is poor, and the laser was found to drift significantly in frequency over a period of minutes.

Once the measurements were completed for a given scattering angle, the analyser was moved to a new angle and the input lens and deflectors optimized once more onto the superelastic signal. The procedure described above was then repeated, until a full set of data was obtained over the complete range of scattering angles accessible to the spectrometer.

Calibration of the absolute angle of the analysers was obtained by directing a beam from a laser diode along the rotation axis of the electron gun, and moving the analysers until this beam passed cleanly through defining apertures located in the analysers. This point corresponded to a scattering angle $\theta_e = 90°$. The relative positions of the analysers were then determined by counting the teeth on the turntable drive gears inside the spectrometer to which the analysers were attached. This angle was then calibrated against the sensors used to externally determine these relative angles [51] with an accuracy of $\pm 0.1°$. It should be noted that the acceptance angle of the analysers was $\pm 3°$, and so it is this that dominates the uncertainty in the measurements.

The laser power was monitored during these experiments using a Newport 1815-C calibrated power meter. The power of the laser beam was maintained at 110 $\pm$ 5 mW at the window to the spectrometer throughout the experiments.

4. Derivation of the ACPs and Stokes parameters

The linear ACPs and pseudo-Stokes parameters were determined by rotating the incident laser beam polarization vector around the scattering plane while monitoring the superelastic signal.

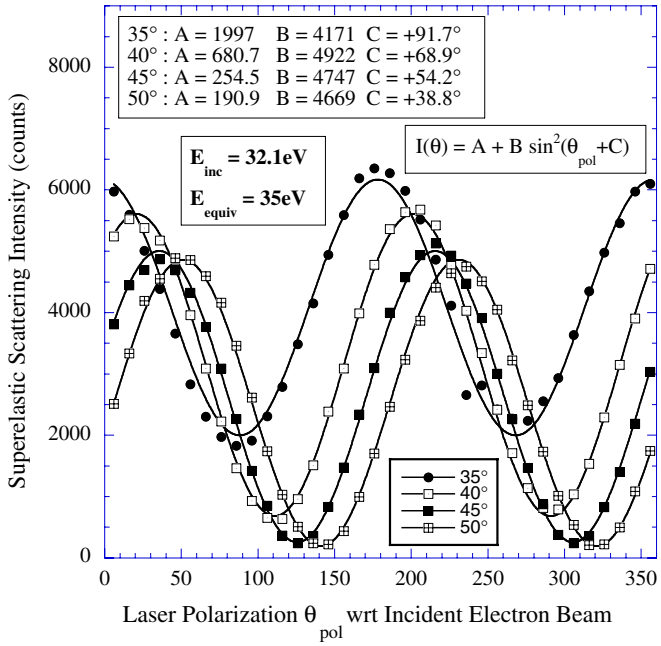

Figure 6. Examples of the superelastic scattering data taken for linearly polarized incident radiation at an incident energy of 32.1 eV (35 eV equivalent energy) for scattering angles from $\theta_e = 35°$ to 50°. Zero degrees is defined as the direction of the incident electron beam. The data was taken by rotating a $\lambda/2$ plate so that the laser polarization vector rotated 360° around the scattering plane. The fitting function parameters are shown.

An example of the results obtained from this configuration are shown in figure 6. The zero polarization angle was defined for all measurements as the direction of the incident electron beam, and so as the analyser rotated around the scattering plane, the direction of the natural frame quantization axis also rotated. All results were taken using analyser 2, as this analyser was set to positive scattering angles as defined in figure 1. Further, the superelastic signal from analyser 2 was much better resolved than from analyser 1.

From figure 6 it is clear that the signal can be fitted to an offset sinusoidal curve. It was decided to use a function of the form:

$$I^{\text{super}}(\theta_{\text{pol}}) = A + B\sin^2(\theta_{\text{pol}} + C) \tag{7}$$

to fit to the data, where A is the offset, B is the amplitude of the sinusoidal function and C is the relative phase of the signal taken with respect to the incident electron beam direction. This function contrasts slightly with that used by Zetner and colleagues [16], who used a co-sinusoidal function with an argument of $2\theta_{\text{pol}}$.

It can be shown that by using this functional form in this geometry, the linear ACPs can be directly related to the parameters A, B and C which are obtained from a non-linear least squares fit to the data. A Marquardt method was used to fit to the data, the co-variance matrix from this fitting routine giving the estimated uncertainty in the fitted parameters. The fitting was conducted using the program Kaleidagraph [56], which has the advantage that the partial derivatives of the fitting parameters is directly input to the program to aid optimization of the least squares fit. This contrasts with many other commercial programs that estimate the derivates from the data, and so do not provide as robust a fit. The data can be seen to vary around the fitted function, and this is principally due to drift in the laser frequency during

data collection as discussed above. By taking data at 36 different polarization angles for each scattering angle as noted above, the effect of this frequency drift on the fit was minimized.

The linear ACPs and Stokes parameters can be related to the fitting parameters using the following relations:

$$\begin{aligned} P_{\rm lin}^{+} &= \frac{B}{2A+B} \\ \gamma^{+} &= \theta_{\rm e} + C + n\frac{\pi}{2} \\ P_1 &= \frac{B}{2A+B}(1 - 2\cos^2(\theta_{\rm e} + C)) \\ P_2 &= \frac{-2B}{2A+B}(\cos(\theta_{\rm e} + C)\sin(\theta_{\rm e} + C)) \end{aligned} \tag{8}$$

where γ^{+} is defined by the relative sign of (P_1, P_2) so as to constrain γ^{+} between $\pm 90^\circ$ as the P-state evolves around the scattering plane. If P_1 is positive, then $n = 0$. If P_1 is negative, then $|n| = 1$ and n takes the same sign as P_2.

The relative uncertainties in these parameters can be determined using an error analysis in the usual way. The uncertainty in $P_{\rm lin}^{+}$ is given by the relative magnitudes A and B obtained from the fit, and since there were 36 data points taken five times for each measurement, the uncertainty in this parameter is much smaller than if $P_{\rm lin}^{+}$ was determined from the Stokes parameters P_1 and P_2. The uncertainty in γ^{+} is given by the uncertainty in C and $\theta_{\rm e}$, which for all measurements was less than 1%. Hence the overall uncertainty in this parameter is taken to be the accuracy to which the polarization vector can be determined with respect to the incident electron beam direction, estimated as $\pm 3^\circ$.

The uncertainty in P_1 and P_2 was determined from the accuracy in all fitting parameters, together with the uncertainty in the absolute determination of the polarization vector with respect to the incident electron beam direction. It was this latter uncertainty which was the dominant contribution to the calculated error bars for these parameters.

The $L_{\perp}^{+}$ collision parameter and the Stokes parameter P_3 are directly related to each other as given by equation (6), and so both were determined simultaneously. These parameters were measured by rotating the $\lambda/4$ plate to the angles $\vartheta_{45^\circ}^{\rm ret}$, $\vartheta_{135^\circ}^{\rm ret}$, $\vartheta_{-45^\circ}^{\rm ret}$, $\vartheta_{-135^\circ}^{\rm ret}$ and measuring the superelastic scattering yield for 30 s over ten different intervals to establish an uncertainty in the measurements. The measurements at $\vartheta_{\pm 45^\circ}^{\rm ret}$ were then combined with those at $\vartheta_{\mp 135^\circ}^{\rm ret}$ and the P_3 parameter with its associated uncertainty was determined from equation (1).

The parameter $P_{\rm tot}^{+}$ which determines the degree of coherence in the interaction was derived from the Stokes parameters P_1, P_2 and P_3 using equation (6). To ensure that radiation trapping was not contributing to this parameter, all measurements were conducted at an oven temperature of 560 °C where the polarization of the fluorescence was measured to be $98 \pm 3\%$, and the signal to noise ratio was high. To further ensure that the effects of radiation trapping were negligible at this temperature, the oven was cooled slowly while the Stokes parameters and fluorescence polarization were measured. No change in the Stokes parameters or ACPs were observed within the uncertainty of the measurements down to an oven temperature of 460 °C. Below this temperature the atomic beam density was so small that no superelastic signal could be observed. From these findings, we conclude that the effects of radiation trapping were negligible at the operating temperature of 560 °C.

4.1. Results and discussion

Figure 7 shows the results of these measurements for an incident energy equivalent to 35 eV, together with calculations from the RDWA model of Stauffer and colleagues [43, 44].

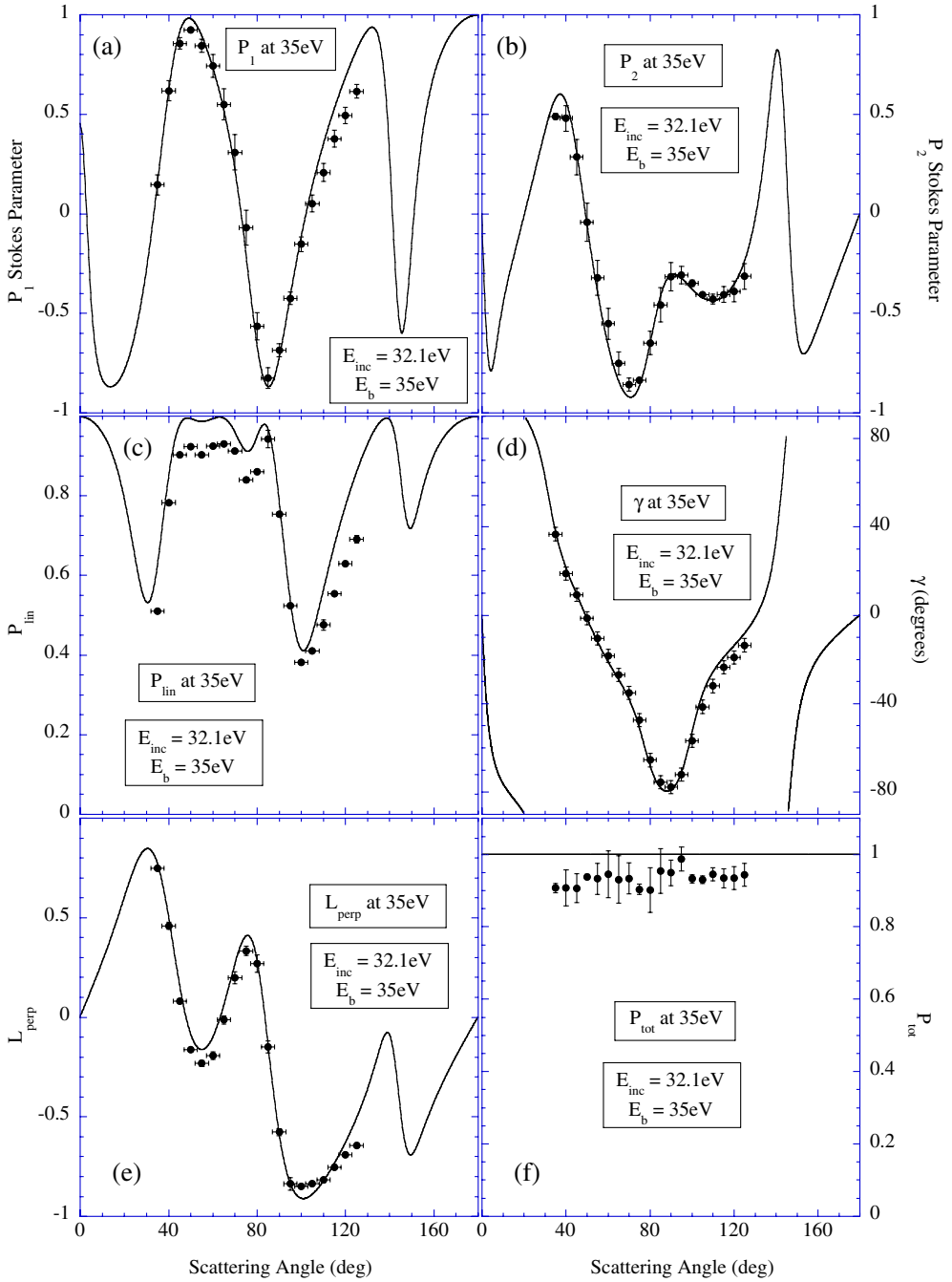

Figure 7. Stokes and ACPs taken at 32.1 eV (35 eV equivalent energy for coincidence measurements) as a function of scattering angle. The results of the RDWA theory of [43, 44] are also shown. Graphs (a) and (b) show the P_1, P_2 Stokes parameters, graphs (c) and (d) the $P_{\rm lin}^{+}$, γ^{+} ACPs and graphs (e) and (f) the $L_{\perp}^{+}$, $P_{\rm tot}^{+}$ parameters. For details, see text.

M Supplementary data files are available from stacks.iop.org/JPhysB/36/4889

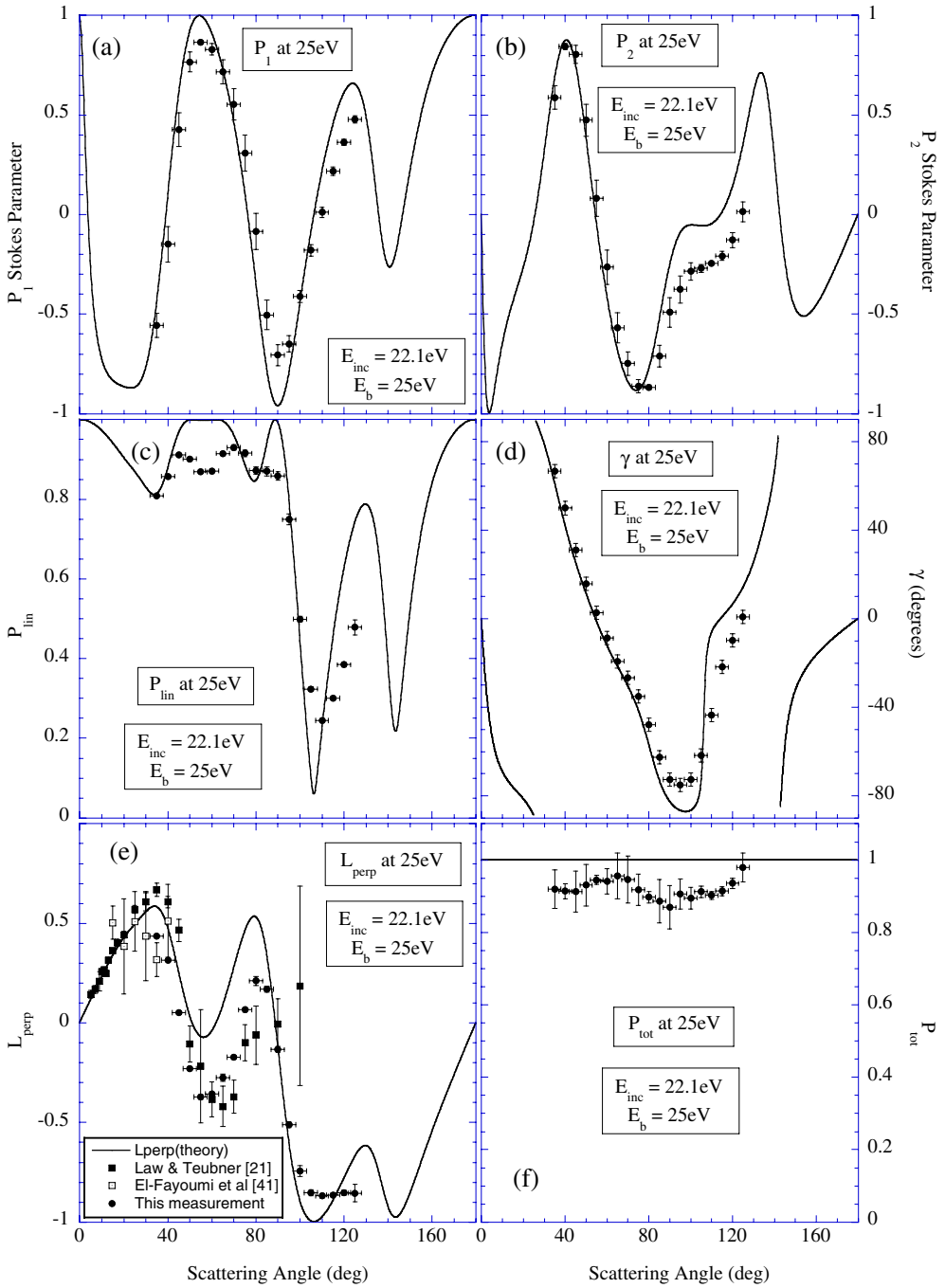

Figure 8. Stokes and ACPs taken at 22.1 eV (25 eV equivalent energy for coincidence measurements) as a function of scattering angle. The results of the RDWA theory of [43, 44] are shown, together with the experimental results of [21] and [41]. Graphs (a) and (b) show the P_1, P_2 Stokes parameters, graphs (c) (d) the $P^+_{\rm lin}$, γ^+ parameters and graphs (e) (f) the $L^+_\perp$, $P^+_{\rm tot}$ parameters.

M Supplementary data files are available from stacks.iop.org/JPhysB/36/4889

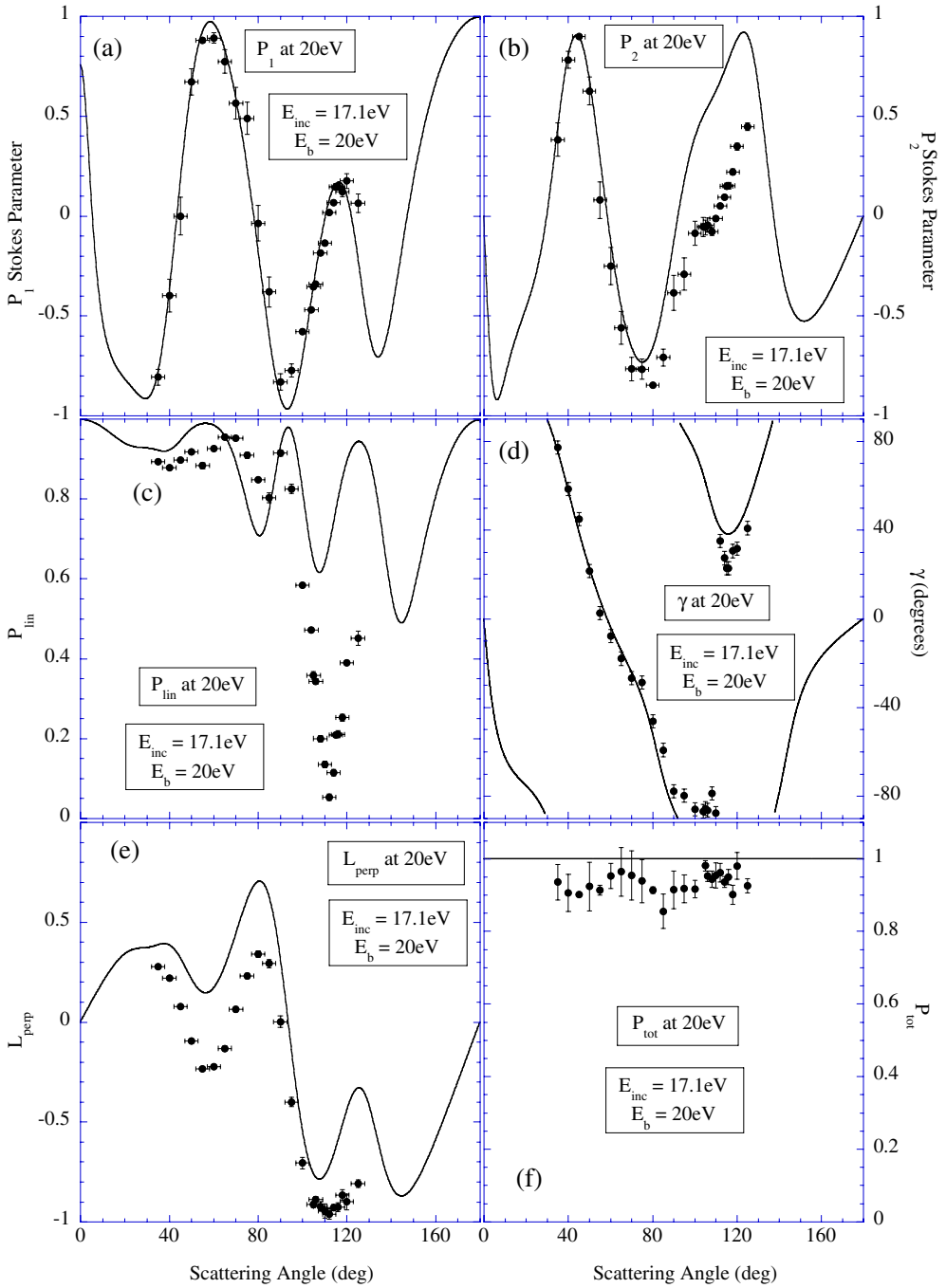

Figure 9. Stokes and ACPs taken at 17.1 eV (20 eV equivalent energy for coincidence measurements) as a function of scattering angle. The results of the RDWA theory of [43, 44] are also shown. Graphs (a) and (b) show the P_1, P_2 Stokes parameters, graphs (c) and (d) the $P_{\rm lin}^{+}$, γ^{+} parameters and graphs (e) and (f) the $L_{\perp}^{+}$, $P_{\rm tot}^{+}$ parameters.

M Supplementary data files are available from stacks.iop.org/JPhysB/36/4889

The theoretical results are shown convoluted with a Gaussian response function representing the angular acceptance of the spectrometer. The experimental results are constrained between the angles $\theta_e = 35°$ and 125° as discussed above, and are taken every 5° at this energy. The uncertainty in the scattering angle is ±3° as determined by the acceptance angle of the analyser lenses.

The Stokes parameters P_1 and P_2 derived from the fits are shown in the top of this figure, whereas the parameters P_{lin}^+ and γ^+ are presented in the middle plots. $L_\perp^+ (= -P_3)$ and P_{tot}^+ are shown in the lower two graphs. The RDWA calculations of [43, 44] are simultaneously plotted against the experimental results for comparison.

The agreement between theory and experiment at this energy is excellent. The Stokes parameter P_1 shows agreement at scattering angles up to $\theta_e = 100°$, at which point there is a slight deviation between experiment and theory. The parameter P_2 agrees well over the whole range of measured angles. The experimental parameter P_{lin}^+ follows the theory in shape, but tends to be slightly lower at scattering angles between $\theta_e = 45°$ and 85° where P_{lin}^+ is predicted to be close to unity. The deviation noted for P_1 at higher scattering angles is also reflected in this parameter.

Agreement between experimental data and theory for the parameters γ^+ and $L_\perp^+$ is very good over all angles where measurements were taken. The uncertainty on the γ^+ parameter is small (±3°) due to the fitting procedure described above, and so this parameter provides a stringent test of the model parameters. The measured uncertainty on $L_\perp^+$ is also low, and the model fits well. There are slight discrepancies at the peaks of this parameter at angles $\theta_e = 60°$, 80° and 100°. This difference is not due to the angular resolution of the spectrometer which has been accounted for in these figures by convoluting the theoretical curves with a Gaussian representing this resolution.

The measured values of P_{tot}^+ at this energy are all seen to be slightly lower than theory, which calculates this parameter to be unity for all scattering angles. Radiation trapping has been eliminated as a possible cause for this discrepancy, and so it can be concluded that there is a small loss of coherence during the interaction. This loss may be due to the spin of the electron changing during the collision, which is not measured here.

Figure 8 shows the measurements taken at 25 eV equivalent energy, compared again to the RDWA calculations of Stauffer and colleagues [43, 44]. The parameter $L_\perp^+$ has also been measured at this energy by Law and Teubner [21] using the superelastic scattering technique, and by El-Fayoumi *et al* [41] using the electron–photon coincidence method. These experimental results are also presented in this figure for comparison.

From these results it is clear that the RDWA model no longer compares as well to experimental data. The general shape is followed, but the magnitudes no longer agree as well as at 35 eV. The results for P_1 again show good agreement at the lower scattering angle, with deviation from theory at the higher scattering angles above 100°. By contrast to the excellent agreement at 35 eV for P_2, the results above 90° at this energy no longer agree. The theoretical calculation shows a saddle at $\theta_e = 110°$ which is similar to the experimental results, however the model overestimates the value of P_2 at this angle.

The differences between theory and experiment seen in the Stokes parameters are reflected in the P_{lin}^+ parameter. The experiment shows a minimum of 0.24 at $\theta_e = 110°$, whereas theory shows a significantly deeper and narrower minimum at $\theta_e = 106°$. These differences are not as significant for the γ^+ parameter, where theory and experiment are in much closer agreement with deviations being seen only at the higher scattering angles.

The parameter $L_\perp^+$ measured here agrees with the experimental results of Law and Teubner [21] and El-Fayoumi *et al* [41] within two standard deviations. The trend in this parameter as a function of scattering angle is very similar for all experimental measurements.

At scattering angles up to $\theta_e = 45°$ the theoretical curve passes through the experimental data. However the minimum predicted at $\theta_e = 60°$ is found to be significantly deeper, and is displaced to a slightly higher angle. The peak positioned at $\theta_e = 80°$ is predicted well, but the magnitude is too high. The variation near $\theta_e = 120°$ is close in magnitude to the data, but the predicted minimum of $L_\perp^+ = -1$ is not observed.

The parameter P_{tot}^+ is again predicted to be unity over all scattering angles. This contrasts with the measurements which again are lower than unity, although the error bars derived from the Stokes parameters reach unity within two standard deviations for most angles. The results again indicate a slight loss of coherence in the scattering process.

The most interesting contrast between theory and experiment is provided by the results at 20 eV equivalent incident energy as shown in figure 9. In this case, the P_1 parameter agrees well with theory, however the P_2 parameter shows large deviations at higher scattering angles. During these experiments it was observed that the magnitude of the B parameter in equation (7) decreased rapidly to a very low value at angles around $\theta_e = 110°$, and so this region was studied in more detail. Data were taken every 2° around this angle, and the results of this study are most easily seen in the parameter P_{lin}^+. A deep and narrow dip is observed in this parameter with a minimum of $P_{lin}^+ = 0.05 \pm 0.01$ at $\theta_e = 112°$. The narrowness of the dip indicates that the minimum is likely to be zero if the experimental resolution is de-convolved from the experimental data.

The RDWA calculation shows a minimum near $\theta_e = 112°$, but does not reproduce the depth nor narrowness of the measurements. This is not surprising, as the RDWA theory is a high energy calculation and is not expected to do as well at lower energies. By contrast, the results for γ^+ agree well for scattering angles below $\theta_e = 90°$, whereas the experimental data shows a 'knee' between $\theta_e = 90°$ and 110°, before rapidly changing to again agree well with theory beyond $\theta_e = 112°$. The fit to the data at these angles is well defined, and so this 'knee' in the γ^+ parameter is considered to be real.

Calculation of the parameter $L_\perp^+$ at this energy is in poor agreement with experiment in magnitude, but the general shape is reasonably well predicted. The experimental results for $L_\perp^+$ shows a definite trend as the energy is lowered, as can be seen by comparing figures 7–9. In particular, the results near $\theta_e = 110°$ show a definite trend towards the state being completely oriented ($L_\perp^+ = -1$) in this region as the energy is lowered.

Finally, the parameter P_{tot}^+ at this energy is still less than unity, although more of the error bars reach unity compared to higher energies. This implies that the interaction becomes more coherent as the energy is lowered. It would be instructive to reduce the energy still further to test whether this trend continues. Attempts were made to collect results at energies lower than 20 eV, but it was found that the electron gun would not focus sufficiently well to prevent scattering from metal surfaces near the interaction region, which prevented the superelastic signal from being observed. The spectrometer was also found to be unstable at lower energies due to scattered electrons charging surfaces near the interaction region which were coated with calcium.

5. Conclusion and future work

It is hoped that these new results will promote further study using different theories. Models such as the CCC theory (see [57] and references therein) have been found to accurately reproduce the ACPs for many targets, including the alkali atoms and helium at low energies. At lower energies the results contrast sufficiently with the RDWA calculations to provide a challenge for models more appropriate at low energies. In particular, the deep minimum in P_{lin}^+ at 20 eV, together with the constraints due to the low uncertainties in these measurements will provide a rigorous test-bed.

The close reproduction of these results by the RDWA theory at 35 eV implies this model is successfully incorporating most of the important physics in the interaction process. The experiment cannot presently measure beyond $\theta_e = 125°$, and to complete the analysis of this scattering process it would be beneficial to make measurements at angles up to $\theta_e = 180°$. At these higher angles the electron deeply penetrates into the atom, and so the scattering becomes increasingly sensitive to both the phase and magnitude of the contributing scattering amplitudes. The results near $\theta_e = 125°$ show a slight deviation from theory even at 35 eV, and it would be instructive to see if this deviation becomes significant beyond this angle. To facilitate these measurements, an experiment is to be set up using the 'magnetic angle changer' invented at Manchester, which allows measurements to be made over the complete set of scattering angles from 0° through to 180° [58]. A complete determination of the ACPs will then be made.

Finally, it should be noted that measurements have also been conducted for the ionization of calcium at incident energies ranging from 10 eV through to 65 eV [40]. Theories such as the CCC model naturally produce results for both excitation and ionization, since they invoke pseudo-states in the continuum and therefore can also calculate the probability of ionization as a function of scattering angle [59]. The range of energies used in these ionization studies encompasses the region where the RDWA model has been shown to be successful for excitation, and it will be interesting to see whether these models will be successful for both excitation and ionization.

Acknowledgments

The Engineering and Physical Science Research Council is gratefully acknowledged for providing the funds to carry out this research. We would also like to thank Dave Coleman and Alan Venables for providing superb technical support for this research programme.

References

[1] Andersen N, Gallagher J W and Hertel I V 1988 *Phys. Rep.* **165** 1
[2] Andersen N and Bartschat K 1996 *Adv. At. Mol. Phys.* **36** 1
[3] Eminyan M, MacAdam K B, Slevin J and Kleinpoppen H 1974 *J. Phys. B: At. Mol. Phys.* **7** 1519
[4] Standage M C and Kleinpoppen H 1976 *Phys. Rev. Lett.* **36** 577
[5] Cvejanovic D, McLaughlin D T and Crowe A 2000 *J. Phys. B: At. Mol. Opt. Phys.* **33** 3013
[6] Cvejanovic D, Clague K, Fursa D, Bartschat K, Bray I and Crowe A 2000 *J. Phys. B: At. Mol. Opt. Phys.* **33** 2265
[7] Andersen N and Bartschat K 1997 *J. Phys. B: At. Mol. Opt. Phys.* **30** 5071
[8] Hertel I V and Stoll W 1974 *J. Phys. B: At. Mol. Phys.* **7** 570
[9] Hertel I V and Stoll W 1974 *J. Phys. B: At. Mol. Phys.* **7** 583
[10] Hertel I V and Stoll W 1977 *Adv. At. Mol. Phys.* **13** 113
[11] Registar D F, Trajmar S, Jensen S W and Poe R T 1978 *Phys. Rev. Lett.* **41** 749
[12] Herman H W and Hertel I V 1982 *Comment At. Mol. Phys.* **12** 61
[13] Scholten R E, Anderson T and Teubner P J O 1988 *J. Phys. B: At. Mol. Opt. Phys.* **21** L473
[14] Teubner P J O, Scholten R E and Shen G F 1990 *J. Mod. Opt.* **37** 1761
[15] Farrell P M, MacGillivray W R and Standage M C 1991 *Phys. Rev.* A **44** 1828
[16] Zetner P W, Li Y and Trajmar S 1992 *J. Phys. B: At. Mol. Opt. Phys.* **25** 3187
[17] Scholten R E, Shen G F and Teubner P J O 1993 *J. Phys. B: At. Mol. Opt. Phys.* **26** 987
[18] Sang R T, Farrell P M, Madison D H, MacGillivray W R and Standage M C 1994 *J. Phys. B: At. Mol. Opt. Phys.* **27** 1187
[19] Li Y and Zetner P W 1994 *Phys. Rev.* A **49** 950
[20] Li Y and Zetner P W 1994 *J. Phys. B: At. Mol. Opt. Phys.* **27** L293
[21] Law M R and Teubner P J O 1995 *J. Phys. B: At. Mol. Opt. Phys.* **28** 2257
[22] Teubner P J O, Karaganov V, Law M R and Farrell P M 1996 *Can. J. Phys.* **74** 984
[23] Karaganov V, Bray I, Teubner P J O and Farrell P 1996 *Phys. Rev.* A **54** R9

[24] Teubner P J O, Farrell P M, Karaganov V, Law M R and Suvorov V 1996 *Aust. J. Phys.* **49** 481
[25] Karaganov V, Bray I and Teubner P J O 1998 *J. Phys. B: At. Mol. Opt. Phys.* **31** L187
[26] Stockman K A, Karaganov V, Bray I and Teubner P J O 1998 *J. Phys. B: At. Mol. Opt. Phys.* **31** L867
[27] Shurgalin M, Murray A J, MacGillivray W R, Standage M C, Madison D H, Winkler K D and Bray I 1998 *Phys. Rev. Lett.* **81** 4604
[28] Shurgalin M, Murray A J, MacGillivray W R, Standage M C, Madison D H, Winkler K D and Bray I 1999 *J. Phys. B: At. Mol. Opt. Phys.* **32** 2439
[29] Hall B V, Shurgalin M, Murray A J, MacGillivray W R and Standage M C 1999 *Aust. J. Phys.* **52** 515
[30] Johnson P V, Spanu C, Li Y and Zetner P W 2000 *J. Phys. B: At. Mol. Opt. Phys.* **33** 5367
[31] Zetner P W, Johnson P V, Li Y, Csanak G, Clark R E H and Abdallah J Jr 2001 *J. Phys. B: At. Mol. Opt. Phys.* **34** 1619
[32] Johnson P V, Spanu C and Zetner P W 2001 *J. Phys. B: At. Mol. Opt. Phys.* **34** 4311
[33] Karaganov V, Teubner P J O, Brunger M J and Slaughter D 2001 *XXII ICPEAC* p 146 (abstracts)
[34] MacGillivray W R and Standage M C 1988 *Phys. Rep.* **168** 1
[35] Farrell P, MacGillivray W R and Standage M C 1988 *Phys. Rev.* A **37** 4240
[36] Murray A J, Woolf M B J and Read F H 1992 *J. Phys. B: At. Mol. Opt. Phys.* **25** 3021
[37] Murray A J and Read F H 1992 *Phys. Rev. Lett.* **69** 2912
[38] Murray A J and Read F H 1993 *Phys. Rev.* A **47** 3724
[39] Hussey M and Murray A J 2002 *J. Phys. B: At. Mol. Opt. Phys.* **35** 3399
[40] Murray A J and Cvejanovic D 2003 *J. Phys. B: At. Mol. Opt. Phys.* **36** 4875
[41] El-Fayoumi M A K, Beyer H-J, Shahin F, Eid Y A and Kleinpoppen H 1988 *At. Phys.* **11** 173
[42] Zohny E I M, El-Fayoumi M A K, Hamdy H, Beyer H-J, Eid Y, Shahin F and Kleinpoppen H 1989 *Proc. ICPEAC Conf.* vol 16 p 173
[43] Srivastava R, Zuo T, McEachran R P and Stauffer A D 1992 *J. Phys. B: At. Mol. Opt. Phys.* **25** 3709
[44] Stauffer A D 2003 private communication
[45] McClelland J J and Kelley M H 1985 *Phys. Rev.* A **31** 3704
[46] Meng X K, MacGillivray W R and Standage M C 1992 *Phys. Rev.* A **45** 1767
[47] Whitley R M and Stroud C R 1976 *Phys. Rev.* A **14** 1498
[48] Bevarini N, Giammanco F, Maccioni E, Strumia F and Vissani G 1989 *J. Opt. Soc. Am.* B **6** 2188
[49] Ross K J and Sonntag B 1995 *Rev. Sci. Instrum.* **66** 4409
[50] Cvejanovic D and Murray A J 2002 *Meas. Sci. Technol.* **13** 1482
[51] Murray A J, Turton B C H and Read F H 1992 *Rev. Sci. Instrum.* **63** 3346
[52] Murray A J 2002 *Meas. Sci. Technol.* **13** N12
[53] Murray A J 2003 *Meas. Sci. Technol.* **14** N72
[54] Brunt J N H, King G C K and Read F H 1977 *J. Phys. B: At. Mol. Phys.* **10** 7
[55] Murray A J, Pascual R, MacGillivray W R and Standage M C 1992 *J. Phys. B: At. Mol. Opt. Phys.* **25** 1915
[56] Kaleidagraph Synergy Software, USA (www.synergy.com)
[57] Bray I, Fursa D V, Kheifets A S and Stelbovics A T 2002 *J. Phys. B: At. Mol. Opt. Phys.* **35** R117
[58] Read F H and Channing J M 1996 *Rev. Sci. Instrum.* **69** 84
[59] Bray I 2003 private communication